Lab on a Chip

PAPER

View Article Online
View Journal | View Issue

Cite this: *Lab Chip*, 2026, **26**, 3493

Flow-programmable and reversible surface-induced LLPS in nanofluidic channels

Ryoichi Ohta, * Zhixin Zhao, Xuan Yan, Ruying Wang and Kazuma Mawatari *

Liquid–liquid phase separation (LLPS) functions as a high-performance reactor strategy in cells, creating dynamic "membrane-less organelles" that selectively concentrate biomolecules. Mimicking this volumetric strategy on a chip offers a route to transcend the capacity and kinetic limits of conventional static surface functionalization; however, engineering applications have been hindered by the stochastic nature of condensate nucleation in bulk mixing. Here, we present "flow-programmable nanofluidic surface LLPS," a method for deterministically and instantaneously inducing and manipulating surface-mediated LLPS condensates by utilizing the high surface area-to-volume ratio of nanochannels. Unlike random bulk formation, the high surface-to-volume ratio in nanochannels ensures exhaustive molecular recruitment, enabling millisecond-scale equilibration and precise thickness programming governed by diffusion-limited transport physics ($\delta \propto Q^{0.3}$). Furthermore, the formed condensates exhibit viscous dewetting dynamics, allowing for flow-tunable manipulation including nm-scale thickness control and reversible hydrodynamic peel-off. The unique properties of these surface LLPS reactors hold the potential to overcome limitations of conventional approaches for functional molecule immobilization on 2D surfaces. Examples include the high-capacity accommodation of functional molecules within 3D condensed phases, the dynamic operation of the reactors themselves, and the implementation of complex interactions such as substrate channeling.

Received 2nd January 2026,
Accepted 23rd March 2026

DOI: 10.1039/d6lc00003g

rsc.li/loc

Introduction

Surface chemical reactions constitute the cornerstone of microfluidic technologies, underpinning applications ranging from high-throughput immunoassays and DNA hybridization to catalytic microreactors.[1,2] In these systems, the device performance—sensitivity, specificity, and reaction rate—is largely dictated by the efficiency of molecular interactions at the solid–liquid interface. To maximize this efficiency, extensive efforts have been devoted to optimizing the engineered surface. Strategies include high-density molecular packing using self-assembled monolayers (SAMs) to increase probe capacity,[3] and orientation control of capture proteins (*e.g.*, using protein G or linker chemistry) to ensure active binding sites face the solution.[4] Additionally, passive mixing structures, such as herringbone ridges,[5,6] are often integrated to overcome mass-transport limitations in microchannels.

While these chemical and structural modifications improve performance, a more fundamental approach to enhancing interfacial interaction is to geometrically scale down the fluidic confinement itself. This leads to the domain of nanofluidics (typically 10^1–10^2 nm channel dimensions). As comprehensively reviewed by several groups, transport phenomena in this regime are dominated by the extremely high surface-to-volume (S/V) ratio and rapid radial diffusion, creating a unique environment where surface effects govern the bulk fluid behavior.[7,8] Our group has attempted to utilize nanofluidics as a reactor. By employing immunochemical reactions on the surface of nanochannels, we can capture introduced molecules 100%,[9] and the reaction completes instantaneously.[10] Enzyme reactions proceed rapidly in nanochannels.[11]

Despite these advances, the "solid–liquid interface" paradigm faces intrinsic physical limitations inherent to its static, two-dimensional nature. First, functional molecules are confined to a single plane, where steric hindrance and rapid saturation impose an upper limit on the effective probe density.[12] Second, the static immobilization restricts molecular mobility, impeding the implementation of complex multi-body interactions—such as substrate channeling in enzymatic cascades—that rely on dynamic cooperation between multiple molecules.[13] Third, conventional surface chemistries are typically permanent; dynamic operations such as removing, exchanging, or replenishing the functional layer on demand are difficult to achieve. These constraints stem from the paradigm of static 2D surfaces. A potential breakthrough may lie in

Waseda University, 2-7 Hibikino, Wakamatsu-ku, Kitakyushu, Fukuoka 808-0135, Japan. E-mail: ohta.ryo@aoni.waseda.jp, kmawatari@waseda.jp

shifting the reaction paradigm from a static 2D monolayer to a dynamic, volumetric 3D phase.

In contrast to artificial 2D surfaces, biological systems utilize liquid–liquid phase separation (LLPS) to organize cellular biochemistry.[14,15] Analogous to the demixing of oil and water, LLPS occurs when multivalent, weak interactions among macromolecules induce a homogeneous solution to spontaneously separate into two distinct aqueous phases: a dilute phase and a dense, polymer-rich phase. This process creates "membrane-less organelles" that function as "volumetric (3D)" liquid reactors capable of selectively enriching specific biomolecules by orders of magnitude while preserving liquid-like mobility.[16,17] This state plays a crucial role in diverse functions, from gene expression to tumor biology,[18] by enabling high-capacity storage and dynamic regulation.[19] Crucially, recent studies have revealed that biological LLPS is not solely a bulk phenomenon but is often nucleated and regulated by surfaces, such as cell membranes.[20,21] These "surface-associated condensates" suggest that surfaces can act as powerful scaffolds to stabilize and organize liquid phases. The unique state of LLPS —a three-dimensional condensed phase possessing liquid-like mobility, where molecules freely collide and diffuse —suggests transformative possibilities for engineering: if this biological "dynamic liquid reactor" strategy could be reproduced and controlled on a microchip, it would serve as a next-generation platform capable of breaking through the limitations of conventional solid surface modifications—specifically saturation, irreversibility, and restricted reaction kinetics.

However, the formidable barrier to exploiting LLPS as a programmable reactor lies in the precise spatiotemporal control of phase separation—specifically, generating the condensate exactly when and where it is required. Simple bulk mixing of inducing components inevitably leads to nucleation and growth that are stochastically distributed in both space and time. While microfluidic platforms have been extensively employed in this field,[22] previous studies have primarily aimed to elucidate the fundamental scientific principles of LLPS, such as mapping phase diagrams[23] and biophysical characterization,[24,25] rather than engineering the condensate itself as a functional device component. Consequently, these approaches have predominantly relied on passive mixing strategies, resulting in random phase formation. Moreover, attempts to spatially define the phase using surface-immobilized nuclei in microscale channels often fail because the surface-to-volume (S/V) ratio is too low; the surface effect is diluted by the bulk volume and is too weak to govern the phase behavior of the entire system.

To overcome this, we refocus on "nanofluidics." The true advantage of utilizing nanospace lies not merely in its minute dimensions but in its overwhelming surface-to-volume (S/V) ratio. For instance, in a nanochannel with a depth of several hundred nanometers, the effective concentration of surface-immobilized molecules relative to the channel volume easily reaches the micromolar (μM) range—a typical threshold concentration required to trigger LLPS for many biomolecules. Consequently, strictly within nanofluidic confinement, the surface transcends its role as a passive "wall" and may function as a "dominant field" capable of dictating the phase transition of the entire liquid volume. Crucially, this confinement ensures that virtually all introduced molecules are exhaustively recruited into the condensed phase, preventing the "sample bypass" common in larger microfluidic channels. Equally important is the timescale of mass transport. Nanoconfinement drastically shortens the diffusion distance, enabling radial mixing to complete on the microsecond scale. This ensures that the formation, growth, and equilibration of the LLPS condensate occur instantaneously, eliminating the kinetic lag often observed in bulk systems. By coupling this rapid equilibration with the principle of "diffusion-limited supply," we hypothesize that the typically chaotic LLPS phase generation can be transformed into a deterministic deposition process. This approach would allow the LLPS film thickness to be programmed with nanometer-to-Ångström precision using a single parameter: flow rate.

In this study, we demonstrate the first realization of flow-controllable surface-induced LLPS inside a nanofluidic channel. Using histone H1 and single-stranded DNA (ssDNA) as a model system—where H1 was immobilized on the nanochannel surface and the incoming ssDNA was tracked—we observed the formation of a concentrated condensate phase whose thickness was dynamically modulated by the flow velocity. The finding that this film thickness follows a specific scaling law $\delta \propto Q^{0.3}$ suggests that the growth mechanism is strictly governed by boundary-layer transport physics. Notably, the film formation kinetics were remarkably rapid, reaching steady-state equilibrium within milliseconds; this indicates that the nanofluidic confinement facilitates instantaneous capture and phase transition, overcoming the stochastic nucleation and slow maturation times often seen in bulk LLPS. Furthermore, the formed films exhibited viscous dewetting behavior, allowing for reversible transport by hydrodynamic shear. Consequently, this work establishes a platform for creating reversible, flow-tunable, and volumetric reaction fields, bridging the gap between static surface chemistry and dynamic biological organelles. While "organ-on-a-chip" systems are now prevalent,[26] we envisage that this technology will contribute to the realization of "organelle-on-a-chip" systems capable of reconstructing subcellular reaction environments.

Experimental

Experimental concept

A conceptual illustration of the nanofluidic LLPS demonstration is shown in Fig. 1. Histone H1 was selected as a surface-bound LLPS-inducing molecule because it strongly interacts with single-stranded DNA (ssDNA) *via* electrostatic attraction and is known as a key regulator of chromatin condensation.[27] The phase behavior of the H1–DNA system in bulk has been reported, indicating that micromolar-order concentrations are required for LLPS formation. Although spatial patterning of histone H1 would enable controlled LLPS induction, the present study focuses on fundamental characterization; therefore, the

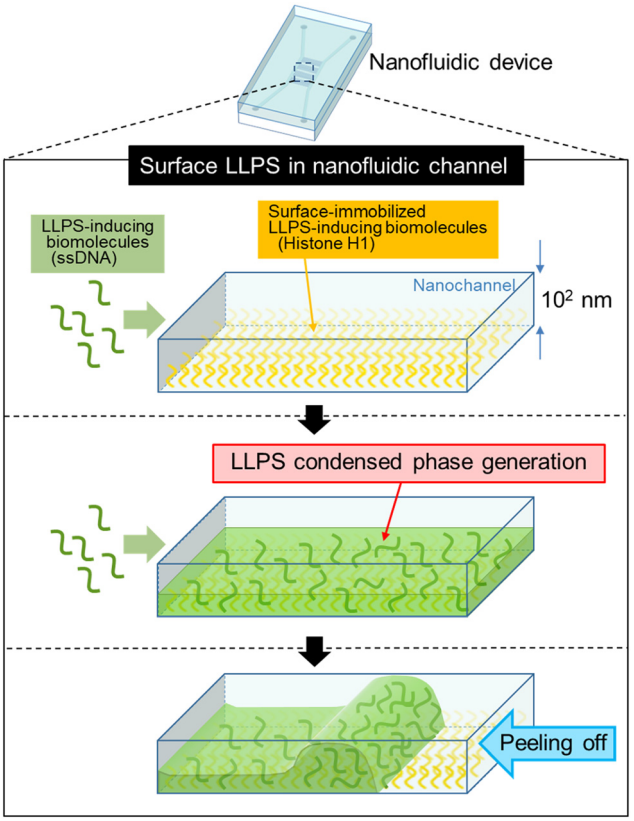

Fig. 1 Conceptual illustration of the formation and flow-driven release of a surface LLPS phase in a nanofluidic channel. Single-stranded DNA (ssDNA) molecules introduced into the channel interact with surface-immobilized histone H1 molecules to form a condensed LLPS phase along the channel wall. The condensed phase maintains fluidity and can be detached by flow-induced shear ("peeling off"), enabling dynamic surface reactions and reconfigurable concentration control within the nanofluidic environment.

entire inner surface of the nanochannel was uniformly coated with histone H1. Fluorescent ssDNA was introduced into the nanochannel to induce LLPS in the confined environment. The condensed phase could appear as (i) a thin surface-adhered layer or (ii) a plug-like structure partially filling the channel. To probe these possibilities, the ssDNA flow rate was systematically varied, and the resulting fluorescence profiles along the channel were recorded as a function of the applied pressure. Changes in local fluorescence intensity were used as indicators of the formation and growth of the surface-associated LLPS phase. After LLPS induction, a buffer solution was introduced into the nanochannel to investigate the stability and dynamics of the condensed phase under reversed or reduced flow. The behavior of the condensed domain—whether retained, thinned, displaced, or detached—was monitored using real-time fluorescence imaging. Particular attention was paid to flow-driven "peel-off" events, where the condensed phase separates from the surface and is transported downstream as a mobile front. These experiments were designed to evaluate whether the surface LLPS phase can function as a reversible, flow-reconfigurable unit within the nanofluidic environment.

Fabrication and surface modification of the nanofluidic device

Fig. 2(a) shows the design of the nanofluidic device. Microchannels and nanochannels were fabricated on two separate fused-silica substrates through Cr sputtering, photolithography (FPA-3000i5+, Canon), and reactive ion etching (RIE-101iPH, Samco). Specifically, the microchannels (500 μm wide and 5 μm deep) were fabricated on one substrate. The other substrate was designed to contain arrays of 2 mm-long nanochannels with varying widths (550, 650, 750, 850, and 950 nm, with 20 channels per width). However, all experiments in this study were conducted exclusively using the 750 nm-wide channels. As characterized in Fig. S1, the actual dimensions of the utilized nanochannels were determined to be 750 nm in width and 890 nm in depth. Finally, these two structured substrates were tightly bonded following piranha cleaning and oxygen plasma surface treatment. Upon bonding, the regions where the 2 mm-long nanochannels overlap with the deeper microchannels cease to function as nanoconfinements. Consequently, the final effective length of the nanochannels is strictly defined by the distance between the two parallel microchannels, which is exactly 1 mm, successfully yielding the enclosed nanofluidic device shown in Fig. 2(b).

The immobilization of biomolecules onto the glass surfaces of the nanochannels followed our previously established framework.[9,10] This procedure fundamentally consists of two sequential steps: the aminosilanization of the bare glass surface and the subsequent covalent conjugation of these surface amine groups to the primary amines of the target biomolecules *via* a chemical crosslinker. Because this framework relies strictly on covalent bonding throughout both steps, the resulting functionalized layer cannot be detached by typical hydrodynamic shear forces.

For the biomolecules, recombinant histone H1 solution (H10-54 N, containing 50 mM Tris-HCl at pH 7.5 and 150 mM NaCl) was purchased from SignalChem Biotech Inc. Prior to the immobilization and LLPS formation, a desalination procedure was performed to remove the NaCl. Briefly, 500 μL of a 32 μM histone H1 solution was transferred to a 10 kDa molecular weight cut-off membrane filter (Amicon, Merck KGaA) and centrifuged at 10 000*g* for 15 min, reducing the volume to approximately 50 μL. Then, 450 μL of TE (Tris-EDTA) buffer was added. This washing cycle was repeated three times, reducing the final NaCl concentration to ~0 mM, as confirmed by a Na^+ ion sensor (LAQUAtwin, Horiba). For the target molecule, a 15 mer ssDNA (dA15) labeled with fluorescein isothiocyanate (FITC) at the 5′ end was purchased from Hokkaido System Science Co., Ltd.

For the first step (surface amination), aminosilanes such as 3-aminopropyltriethoxysilane (APTES) and 3-aminopropyldimethylethoxysilane (APDMES) are commonly used. In this study, a liquid-phase reaction of APDMES (Merck KGaA) was adopted to strictly prevent channel clogging, as its single ethoxy group effectively avoids the 3D polymerization often associated with tri-alkoxy silanes. The modification protocol was as follows. A 1% (v/v) APDMES solution in

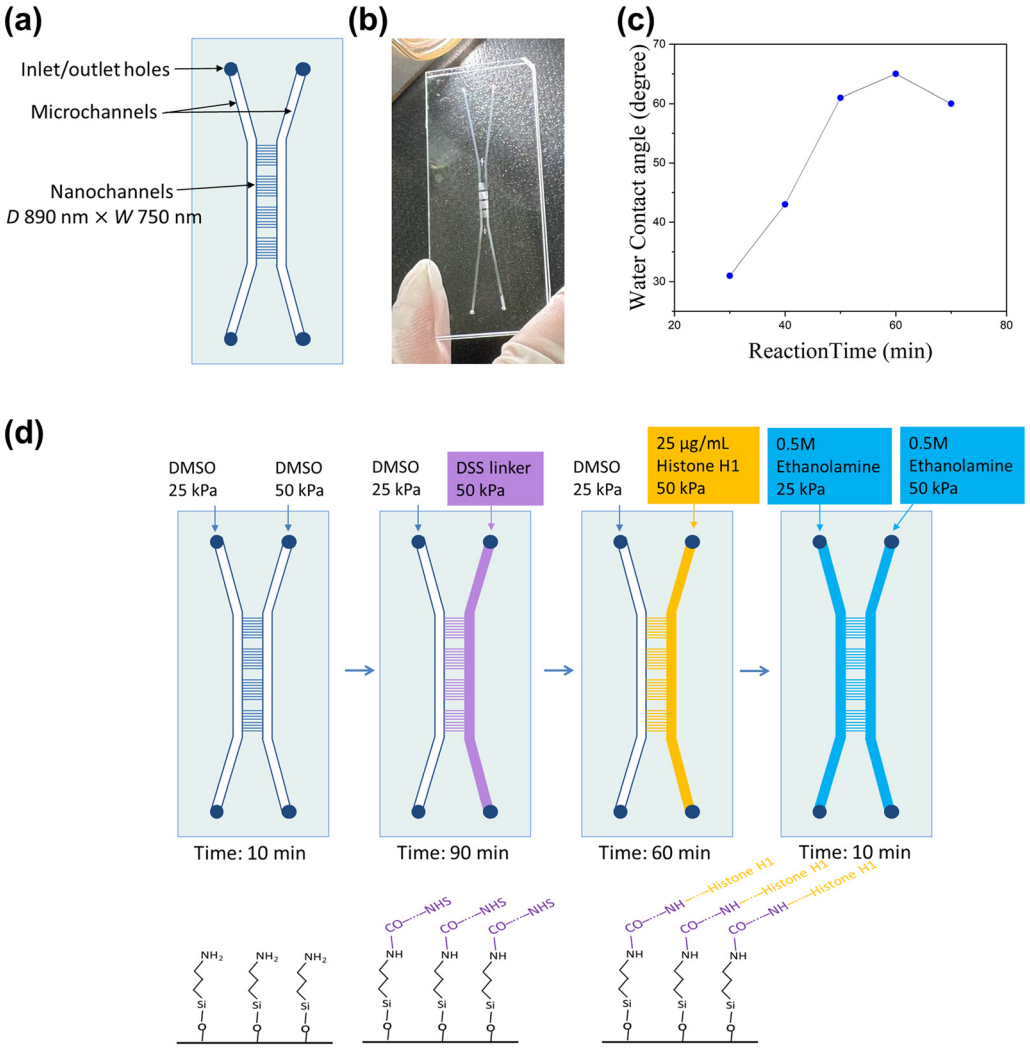

Fig. 2 Fabrication and surface modification of the nanofluidic device. (a) Schematic layout of the device consisting of microchannels and an array of nanochannels (width: 750 nm, depth: 890 nm). (b) Photograph of the glass nanofluidic device after thermal bonding. (c) Water contact angle of the glass substrate as a function of the reaction time of APDMES, showing the progression of surface silanization. (d) Protocol for histone H1 modification inside the nanochannels. Sequential infusion of DMSO, DSS linker solution, histone H1 (25 μg mL^{-1}), and ethanolamine was performed under controlled pressures, enabling immobilization of histone H1 on the nanochannel surface through amine–NHS ester coupling.

anhydrous toluene was prepared under a nitrogen atmosphere to prevent premature hydrolysis. This solution was introduced into the micro- and nanochannels *via* capillary flow and vacuum filling. The reaction time was pre-optimized using flat glass substrates; as shown in Fig. 2(c), the water contact angle reached a plateau of approximately 60° after a 60 min reaction at room temperature, indicating successful amination. This optimized 60 min reaction was applied to the nanochannels.

For the second step, histone H1 was immobilized onto the aminated surface using disuccinimidyl suberate (DSS), a widely standardized homobifunctional NHS ester crosslinker for primary amine conjugation.[4] First, the channels were washed with DMSO, and 5 mM DSS in DMSO was introduced for 90 min to convert the amine groups to reactive NHS esters. Finally, the histone H1 solution (25 μg mL^{-1}) was introduced to react with the DSS linker for 60 min. The unreacted DSS residues were subsequently capped with 0.5 M ethanolamine.[9,10] The excitation and emission wavelengths of the FITC label are 488 nm and 510–530 nm, respectively.

Confirmation of LLPS in bulk

Prior to nanochannel experiments, a series of LLPS assays was performed to verify the intrinsic phase behavior of the selected biomolecular system (histone H1 and ssDNA) and establish a reliable baseline phase diagram for comparison with the subsequent on-chip results. A critical preparatory step for these experiments was the desalination of the histone H1 protein. Given that the LLPS of this system is driven primarily by electrostatic interactions between the positively charged protein and the negatively charged DNA backbone, the presence of excess salt ions (such as NaCl) would screen these charges and inhibit phase separation. Therefore, the protein solution was thoroughly exchanged

into a salt-free buffer using centrifugal ultrafiltration. A series of experiments was then conducted by mixing the desalinated histone H1 and ssDNA at various concentration ratios to systematically investigate the conditions required for LLPS. The mixed solution was observed under a phase contrast microscope.

LLPS experiment in nanochannels

Using the same setup as for surface modification, reagents and water were introduced into the nanofluidic device *via* pneumatic actuation. Histone H1 was immobilized on the nanochannel surface. LLPS-inducing and non-inducing samples were introduced following the protocol illustrated in Fig. 3. FITC-labeled ssDNA (dA_{15}, 5 μM), which forms LLPS with histone H1, and 5 μM FITC solution, which does not induce LLPS, were used as model analytes.

The left microchannel was filled with either ssDNA or FITC solution, whereas the right microchannel was filled with pure water. Both reservoirs were continuously pressurized so that the solutions in each microchannel were constantly refreshed; because the nanochannel flow was orders of magnitude smaller than in the microchannels, changes in microchannel concentration were negligible. Experiments always began with the nanochannels fully rinsed with water. A positive pressure of 100 kPa was applied to the water reservoir, resulting in a hydrostatic pressure of approximately 50 kPa at the right end of the nanochannels. The sample reservoir was initially held at a lower pressure (10 kPa) producing 5 kPa at the left end, producing a net pressure drop of 45 kPa from right to left and thereby maintaining water flow through the nanochannels.

To introduce the sample into the nanochannels, the pressure applied to the sample reservoir was increased above that of the water reservoir, thereby reversing the pressure gradient across the nanochannels. Various pressure differences, and thus flow rates, were applied to investigate their influence on the transport and accumulation behavior of the analytes.

When the fluorescence distribution reached a steady state and showed no further temporal evolution, the pressure on the sample reservoir was lowered again to re-establish reverse flow of water through the nanochannels. The resulting changes in fluorescence intensity profiles were analyzed to evaluate the dissipation or detachment behavior of condensed phases formed by LLPS.

All LLPS introduction and peel-off experiments were conducted at a stabilized room temperature of 25 °C.

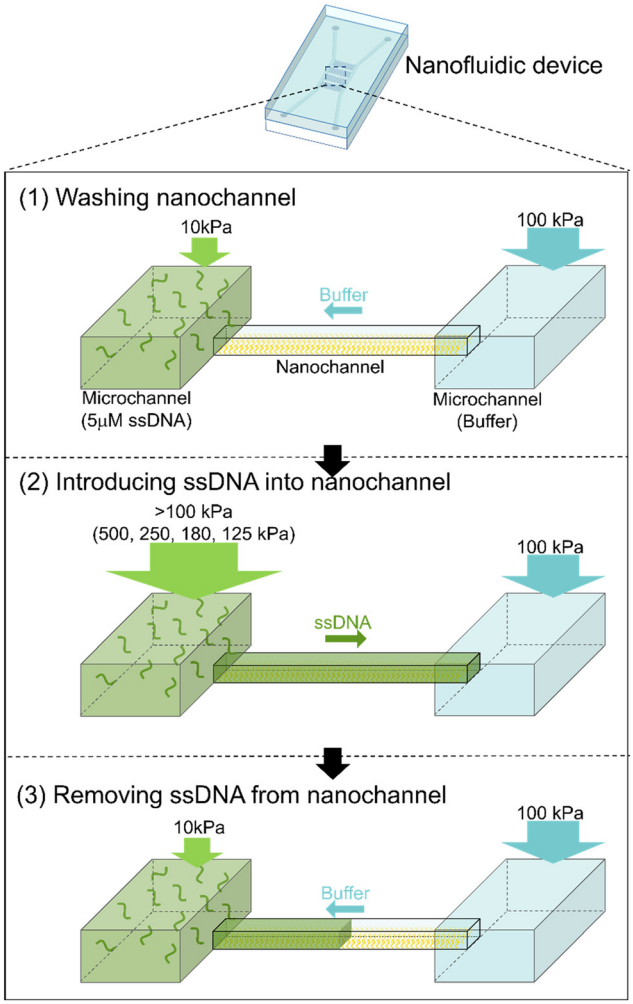

Fig. 3 Experimental protocol for ssDNA introduction and removal in nanochannels. Schematic illustration of the procedure used to introduce LLPS-inducing samples into the nanochannels and subsequently flush them with water. The left microchannel was filled with either FITC-labeled ssDNA (5 μM) or FITC solution (5 μM), while the right microchannel was filled with pure water. Continuous pressurization refreshed the contents of both microchannels, and the nanochannel flow was controlled by adjusting the pressure difference between the two reservoirs. (1) The experiment began with nanochannels fully rinsed by applying a higher pressure to the water reservoir (100 kPa) than to the sample reservoir (10 kPa). (2) Increasing the pressure of the sample reservoir above that of the water reservoir reversed the pressure gradient, introducing ssDNA (or FITC) into the nanochannels at controlled flow rates. (3) After the fluorescence profile reached a steady state, the pressure gradient was reversed again to drive water backward through the nanochannels, enabling analysis of the removal and potential detachment of fluorescence-enriched regions.

Results

Confirmation of LLPS in bulk

The results of bulk LLPS experiments are summarized in Table 1. Droplet-like condensed phase formation was observed under various conditions, confirming that the sample used in this study possesses the activity to induce LLPS. Furthermore, it was found that the trigger for LLPS induction is in the μM

Table 1 Investigation of LLPS formation in bulk

Concentration (protein : DNA)	Reaction time (min)	Result
1 μM : 1 μM	60	No droplet
1 μM : 10 μM	60	Droplet
5 μM : 10 μM	60	Droplet
10 μM : 10 μM	60	Droplet
10 μM : 5 μM	60	Droplet

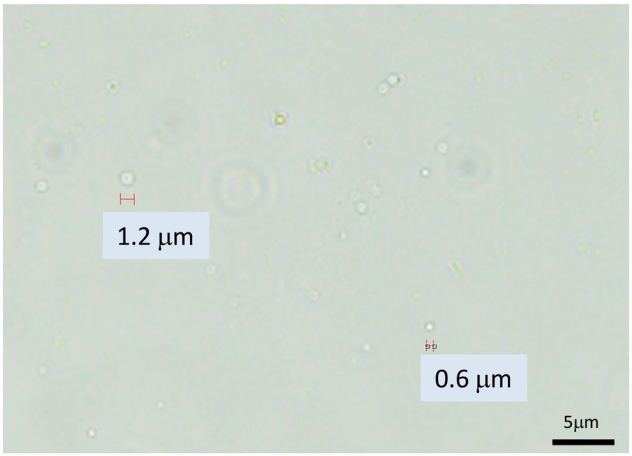

Fig. 4 A result of LLPS in bulk (5 μM histone H1 and 10 μM ssDNA). Droplets observed using a phase-contrast microscope.

order. The results were in good agreement with previously reported results.[21] The droplet size ranged from hundreds of nanometers to several micrometers, as observed with a phase contrast microscope (Fig. 4).

Initial formation of an ssDNA-rich plug at the nanochannel entrance

To investigate the LLPS behavior in nanofluidic channels, the device was first filled with pure water, and fluorescently labeled ssDNA (5 μM) was introduced from the left microchannel. The hydraulic resistances of the upstream/downstream microchannels were designed such that applying 50 kPa to the ssDNA reservoir resulted in a pressure of 25 kPa at the nanochannel entrance, while applying 25 kPa to the water reservoir produced a downstream pressure of 12.5 kPa. Consequently, a driving pressure difference of 12.5 kPa was applied across the nanochannels, under which the ssDNA solution was continuously supplied for approximately 30 min.

During this initial introduction, a bright fluorescence domain emerged at the nanochannel entrance (Fig. S2), eventually forming a cap-like structure that fully blocked flow through the channel. Once this plug formed, reversing the pressure by 100 kPa did not restore flow, indicating a mechanically robust obstruction. A higher reverse pressure of 400 kPa was required to reopen several nanochannels, as confirmed by the reappearance of fluorescent streaks upon introducing FITC solution. Following this rinsing step, the reopened channels remained patent and did not exhibit further blockage during subsequent experiments. All LLPS characterization experiments described below were performed using these opened channels.

FITC introduction into nanochannels

To establish a baseline for transport behavior in histone-modified nanochannels, FITC solution (5 μM), which does not induce LLPS with histone H1, was first introduced into the reopened nanochannels. Fig. 5(a) shows the time-resolved fluorescence images and corresponding intensity profiles after switching the pressure to drive FITC from the left microchannel into the nanochannels. Within the first 2 s (Fig. 5(a), left), the fluorescence front propagated smoothly from left to right, producing a characteristic "wavefront" profile that shifted in a manner consistent with advective transport in nanochannels. After the front reached the right end of the channel (Fig. 5(a), right), the intensity distribution became nearly time-invariant, indicating that a steady-state concentration profile had been established.

A gradual decrease in fluorescence intensity toward the right side of the channel was observed in the steady state. This gradient did not depend on molecular transport but arose from an instrumental factor: to avoid strong stray fluorescence originating from the FITC-filled microchannels, the excitation light was laterally displaced during imaging, resulting in an illumination gradient along the nanochannel axis. The smoothness and stability of the observed intensity profiles therefore indicate minimal influence of surface adsorption or photobleaching under the present conditions.

Fig. 5(b) compares the steady-state fluorescence profiles obtained at three different pressure drops (25, 75, and 100 kPa). The profiles almost completely overlapped, demonstrating that the steady-state concentration in the nanochannel was insensitive to flow rate when the sample concentration in the upstream microchannel was constant. The absence of any flow-dependent enrichment verifies that FITC was transported as a simple solute without detectable interaction with the histone-modified surface. This serves as an essential negative control for distinguishing LLPS-driven accumulation observed in the ssDNA experiments described later.

ssDNA introduction in nanochannels

To examine LLPS-driven accumulation behavior, FITC-labeled ssDNA (5 μM), which forms LLPS with histone H1, was introduced into the nanochannels. Fig. 6(a) shows the time evolution of the fluorescence intensity profiles under a pressure drop of 450 kPa. Similar to the FITC experiments, a fluorescence wavefront propagated from left to right during the first ~10 s. However, in contrast to FITC, the resulting steady-state profiles exhibited pronounced spatial heterogeneity, forming two prominent intensity maxima separated by a distinct trough. The presence of discontinuous or step-like features within the profile cannot be attributed to the illumination gradient observed in the FITC control, suggesting the formation of localized ssDNA-enriched domains associated with surface-induced LLPS.

Fig. 6(b) summarizes the steady-state intensity profiles obtained under different pressure drops. In striking contrast to the FITC case, ssDNA signals increased substantially with pressure, indicating that the amount of ssDNA retained in the nanochannel depended strongly on the applied flow rate. Repeated runs under identical conditions produced similar but not identical profiles, consistent with the stochastic

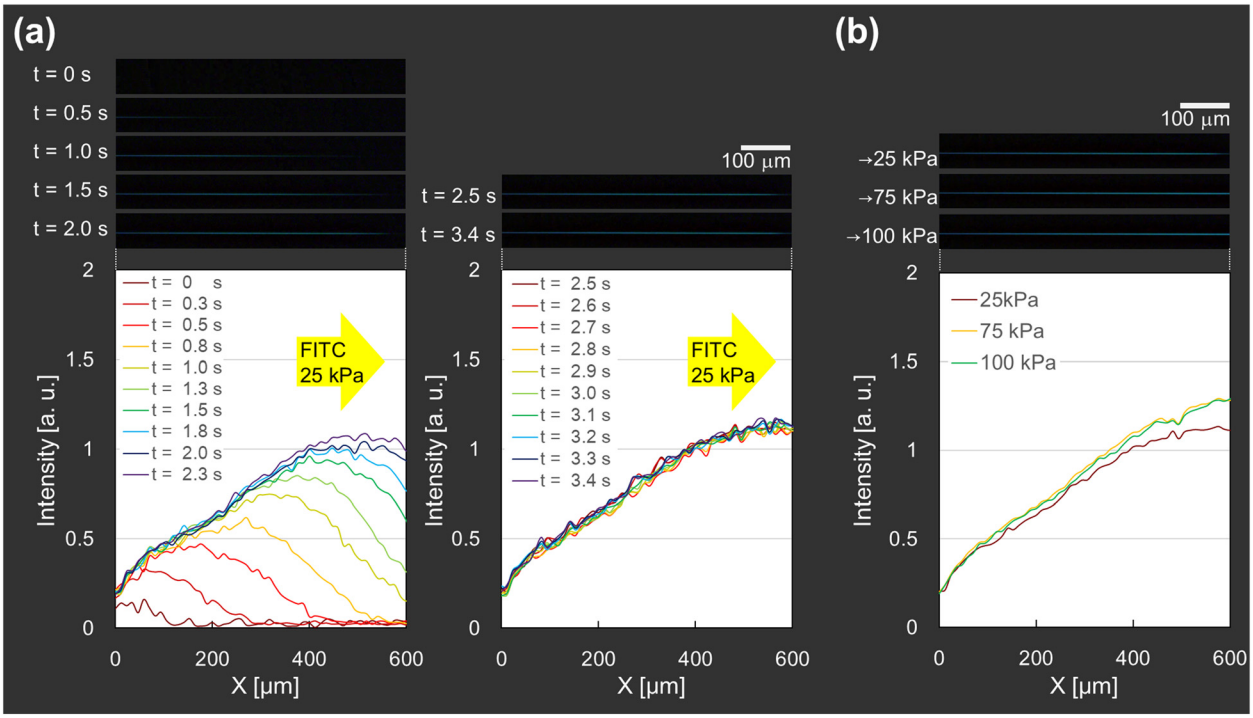

Fig. 5 Transport behavior of FITC in histone-modified nanochannels. (a) Time-lapse fluorescence images (top) and intensity profiles (bottom) during FITC introduction at a pressure drop of 25 kPa. Left: 0–2 s after pressure switching, showing the propagation of a fluorescence wavefront from left to right. Right: 2.5–3.4 s after the front has reached the channel end, illustrating the establishment of a steady-state profile. A gradual decrease in intensity along the *x*-axis originates from an imposed excitation-light gradient used to avoid stray fluorescence from the microchannel. (b) Steady-state fluorescence profiles measured at pressure drops of 25, 75, and 100 kPa. All profiles overlap, demonstrating almost negligible dependence on flow rate and confirming that FITC does not undergo surface accumulation or LLPS-related enrichment in the nanochannels.

nature of LLPS nucleation and domain growth on a heterogeneous surface.

To quantify the pressure dependence, the intensity profiles were integrated along the channel axis (Fig. 6(c)). The integrated fluorescence increased monotonically with pressure. A log–log plot of the same data (Fig. 6(d)) revealed a power-law relationship, $I \propto P^{0.34}$, with an exponent significantly smaller than unity. This sublinear dependence is a hallmark of diffusion-limited mass transport to a boundary layer—consistent with shear-enhanced accretion of a condensed ssDNA/H1 phase rather than simple advective transport. Notably, such behavior was absent in FITC experiments, confirming that the observed pressure dependence originates from LLPS-mediated enrichment at the nanochannel surface.

Notably, the propagation speed of the fluorescence wavefront was drastically lower for ssDNA than for FITC, despite the pressure drop being 18-fold higher (450 kPa *vs.* 25 kPa). Whereas FITC traversed the 600 μm nanochannel within 2 s, ssDNA required approximately 12 s. This sixfold reduction in propagation velocity cannot be explained by differences in viscosity or advective transport. Instead, it suggests that the ssDNA signal is carried not by bulk flow of the aqueous phase but by the shear-assisted advance of a condensed ssDNA/H1 phase adhering to the channel surface.

ssDNA removal from nanochannels (peel-off)

After establishing steady-state fluorescence distributions, the pressure gradient across the nanochannel was reversed to examine the removal behavior of ssDNA. The moment at which water flow from the right microchannel entered the nanochannel was defined as $t = 0$. Fig. 7 compares the removal dynamics of FITC (negative control) and ssDNA (LLPS-inducing sample).

In the case of FITC (Fig. 7, left column), the fluorescence wavefront receded smoothly from right to left. The $t = 0$ profile served as an envelope, and subsequent profiles progressively decreased without exceeding the initial intensity, consistent with simple advective displacement of a dissolved fluorophore. No pronounced local accumulation or deformation of the wavefront was observed.

A markedly different behavior was obtained for ssDNA (Fig. 7, right columns). Before pressure reversal, the fluorescence profile under a 200 kPa forward pressure drop was steady and showed no temporal variation, consistent with a quasi-equilibrium distribution of ssDNA in the nanochannel. Upon reversing the flow, however, the fluorescence front displayed a pronounced bulging deformation near the leading edge. Rather than a simple monotonic retreat, the front transiently increased in intensity and adopted a shape with a distinct protrusion propagating leftward. This behavior suggests

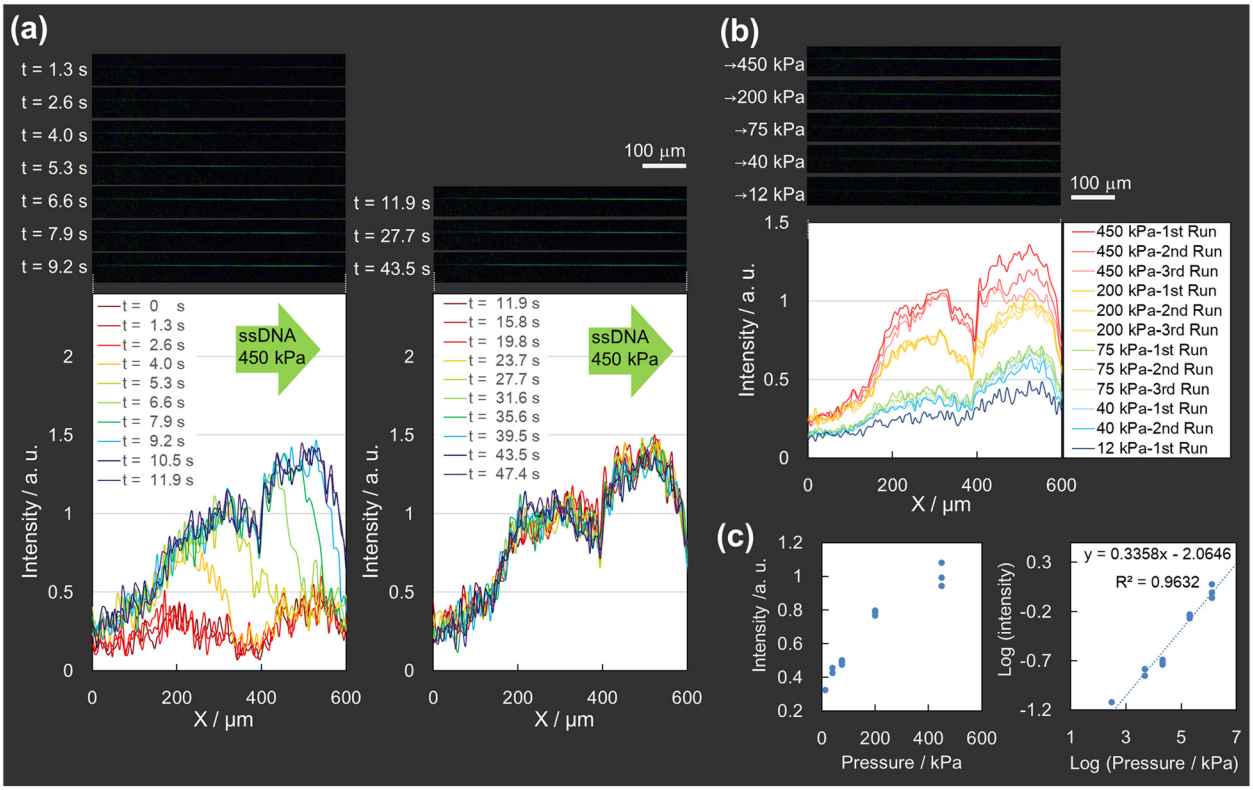

Fig. 6 LLPS-driven accumulation of ssDNA in histone-modified nanochannels. (a) Time-lapse fluorescence images (top) and intensity profiles (bottom) during ssDNA introduction at a pressure drop of 450 kPa. A fluorescence wavefront propagated from left to right (left), after which the profile reached a steady state (right). Unlike FITC, the steady-state distributions exhibit two major peaks and discontinuous features, indicative of localized enrichment associated with LLPS. (b) Steady-state fluorescence profiles obtained at pressure drops ranging from 12 to 450 kPa. Unlike FITC, the ssDNA intensity increased markedly with pressure, demonstrating strong flow-dependent accumulation. (c) Integrated fluorescence intensity as a function of pressure (left) and log–log plot of the same data (right), showing a power-law dependence $I \propto P^{0.34}$ (dashed line), consistent with shear-assisted growth or retention of LLPS-derived condensed domains on the nanochannel surface.

the presence of a cohesive ssDNA-enriched phase that resists immediate displacement and is advected as a deformable entity rather than as a freely dissolved solute. After the front passed and the channel was flushed, the fluorescence intensity returned to a uniformly low level and remained stable.

Such bulging and transient amplification were not observed for FITC and are consistent with the detachment ("peel-off") of a condensed ssDNA/H1 phase from the nanochannel surface. To further examine the robustness of the peel-off behavior, ssDNA introduction was performed under a wide range of pressure drops (12–450 kPa), and the subsequent removal dynamics were measured (Fig. 8). As expected from the results in Fig. 6, the steady-state distributions obtained at t = 0 varied significantly with the introduction pressure, reflecting differences in the amount and spatial organization of the condensed ssDNA/H1 phase prior to flow reversal.

Despite these variations in initial profiles, the removal behavior exhibited a consistent qualitative signature across all tested conditions. In every case, reversing the pressure gradient resulted in the characteristic bulging deformation and transient amplification of the fluorescence front, followed by its leftward propagation and eventual clearance of the nanochannel. This behavior was observed even at the lowest introduction pressure (12 kPa), where the steady-state intensity was relatively small, demonstrating that the cohesive peel-off motion is a general feature of the condensed phase rather than a consequence of a specific loading condition.

In the final column of Fig. 8, the removal pressure was increased (45 → 95 kPa), which approximately doubled the propagation speed of the peeling front while retaining the same qualitative features of bulging and transient amplification. This indicates that the deformation and cohesive motion are not sensitive to the absolute removal pressure but persist as long as a sufficiently strong reverse flow is applied.

For each pressure condition, multiple independent experiments were performed, and the peel-off signatures were reproducibly observed. Representative removal sequences for all conditions are provided as Videos S1–S7.

Discussion

Multiple experimental observations collectively demonstrate that the interaction between fluorescently labeled ssDNA and surface-immobilized histone H1 inside nanofluidic channels results in the formation of a condensed, LLPS-like phase whose

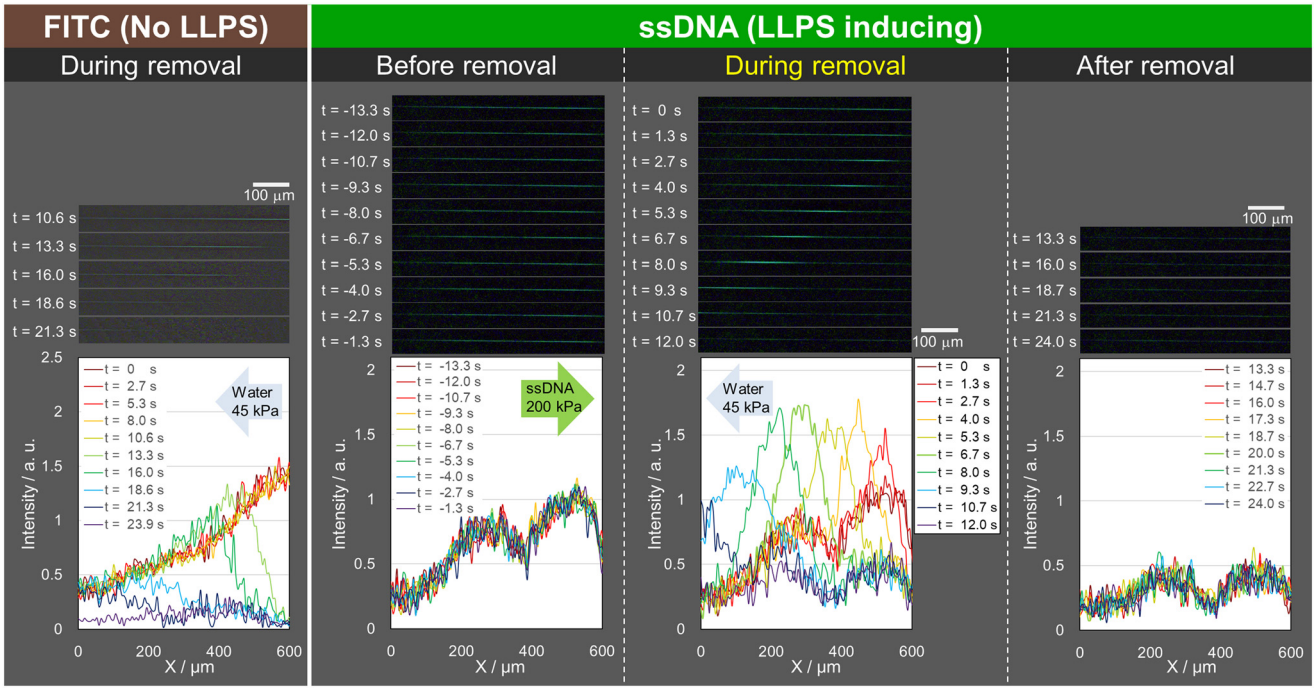

Fig. 7 Removal dynamics of FITC and ssDNA during flow reversal in histone-modified nanochannels. Fluorescence images (top) and corresponding intensity profiles (bottom) after reversing the pressure gradient across the nanochannel (t = 0 defined as the onset of water flow from right to left). Left: FITC (5 μM), which does not induce LLPS. The fluorescence front recedes monotonically, with the t = 0 profile serving as an upper envelope. No local amplification or deformation is observed, consistent with simple advective washout of a dissolved tracer. Center, left: ssDNA (5 μM) immediately before removal, showing the steady-state distribution formed under a forward pressure drop of 200 kPa. Center, right: ssDNA during removal. A pronounced bulging of the leading edge and transient local intensity increase are observed, indicating cohesive motion of a condensed ssDNA/H1 phase rather than diffusive washout. Right: ssDNA after the front has passed, showing uniformly low fluorescence following channel clearance.

morphology, thickness, and transport dynamics depend strongly on the applied flow. By systematically examining steady-state fluorescence profiles, propagation dynamics, pressure-dependent enrichment, and peel-off behavior during flow reversal, we show that the observed phenomena cannot be explained by single-phase hydrodynamics or simple surface adsorption. Instead, the data consistently support a model in which a finite-thickness LLPS condensate forms on the nanochannel wall and behaves as a cohesive entity under shear. Below, we discuss the evidence in increasing order of mechanistic specificity.

1. Steady-state fluorescence profiles indicate multi-phase behavior under nanoconfinement

A first line of evidence arises from the spatial fluorescence profiles obtained during ssDNA introduction (Fig. 6). In sharp contrast to FITC, which produced smooth, monotonic fluorescence distributions consistent with a single freely diffusing solute (Fig. 5), ssDNA consistently exhibited irregular, non-smooth, and sometimes bimodal or discontinuous profiles once steady state was reached.

Because the nanochannel was continuously supplied from the upstream reservoir with a fixed concentration of ssDNA solution, the axial concentration field is expected to remain uniform under all flow conditions. The mean flow velocity during introduction reached the mm s^{-1} range, ensuring that any ssDNA arriving at a given axial position was immediately refreshed by advection. Therefore, in a single-phase system, the steady-state fluorescence profile across the observation window should be smooth and monotonic, although there is a gradient originating from the excitation light intensity distribution.

Importantly, the shape of the profile was preserved across flow rates (Fig. 6(b)): increasing pressure produced a nearly uniform "scalar amplification" of fluorescence without altering the underlying spatial pattern. This behavior is consistent with a model in which each region of the surface has a fixed LLPS propensity determined chiefly by the local density of surface-bound H1, and the thickness of the condensed phase increases with flow rate while preserving this spatial pattern.

2. Propagation-speed analysis reveals formation of an ultrahigh-density condensed phase

A second line of evidence for multi-phase coexistence emerges from the striking disparity between the expected fluid velocity and the observed ssDNA propagation speed. Based on our FITC calibration (Fig. S3), an applied pressure of ΔP = 450 kPa is estimated to generate a rapid axial flow of ~7000 μm s^{-1}. In stark contrast, the ssDNA fluorescence

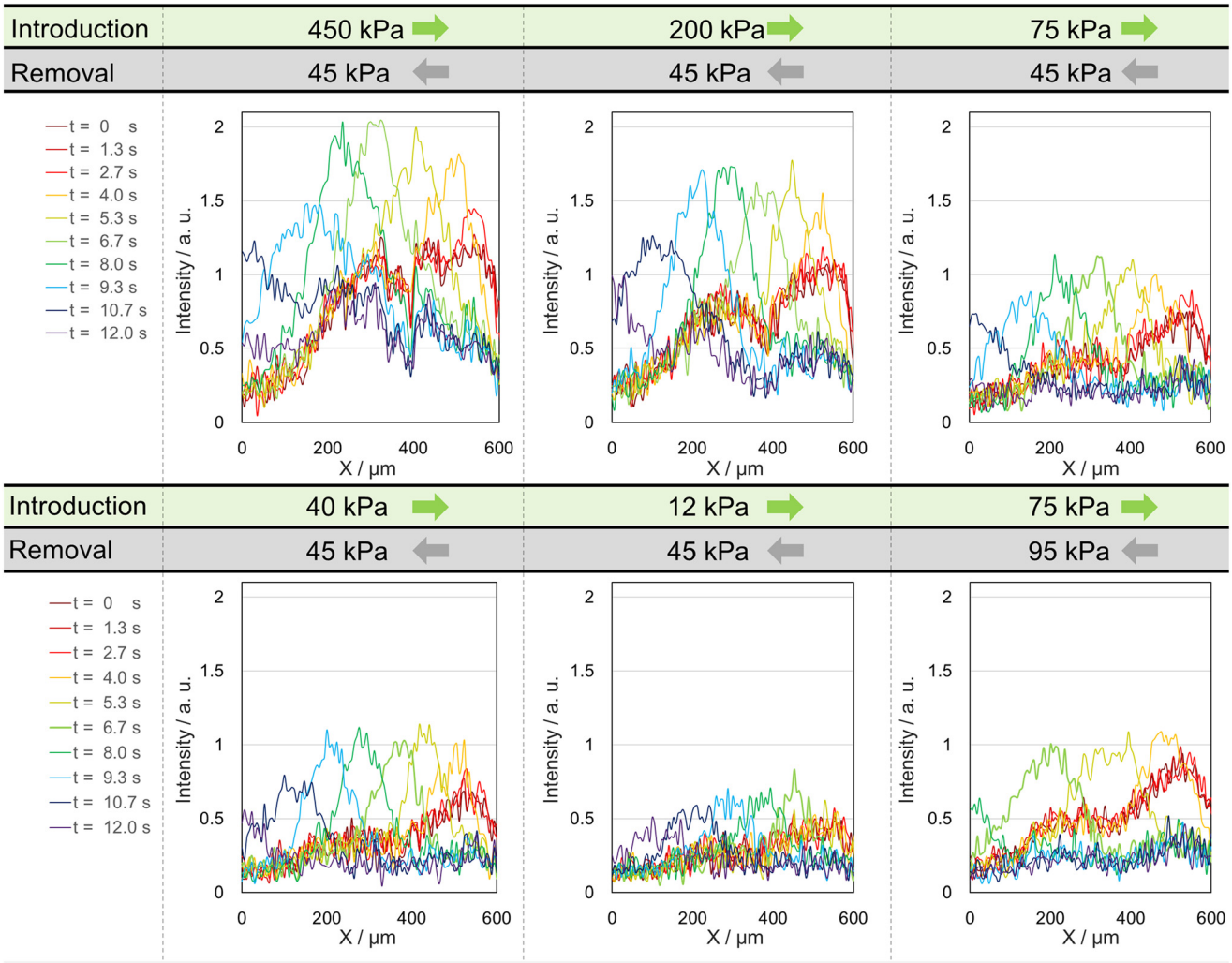

Fig. 8 Peel-off behavior of ssDNA under various introduction and removal pressures. Each panel shows fluorescence intensity profiles during flow reversal (t = 0 to 12 s) after steady-state ssDNA accumulation under a given introduction pressure (12–450 kPa). Although the initial distributions differ substantially among conditions, all cases exhibit a characteristic bulging and transient amplification of the fluorescence front upon pressure reversal, followed by leftward propagation and clearance of the nanochannel. In the rightmost condition, the removal pressure was increased to 95 kPa, resulting in a faster propagation speed while preserving the qualitative features of the peel-off dynamics. Representative datasets are shown; additional repeats demonstrating the reproducibility of the behavior are provided in Videos S1–S7.

front advances at merely ~50 μm s^{-1}. This >100-fold discrepancy cannot be attributed to solution viscosity or partial obstruction of the nanochannel. Instead, a simple material-balance argument reveals that the majority of the injected 5 μM ssDNA is instantaneously sequestered from the freely flowing phase into a condensed phase residing at the walls. For the apparent propagation to slow by this massive factor, the local ssDNA concentration within the characterized 750 nm × 890 nm cross section must be enriched to the order of hundreds of micromolar.

Another possible explanation is that the condensed phase forms a plug-like structure, partially blocking the flow path and causing a slowdown. Assuming the clogging-based explanation, it is difficult to explain the flow velocity dependence of enrichment (Fig. 6(c)) or the fact that the propagation speed during detachment does not depend on the amount of ssDNA accumulation (Fig. 8). These features argue against flow obstruction and instead support a stable two-phase morphology.

Collectively, these features—(i) a >100× slowdown relative to predicted convection, (ii) immediate sequestration implied by sharp leading edges, (iii) pressure-dependent enrichment, and (iv) history-independent detachment kinetics—constitute model-independent evidence for the formation of an ultrahigh-density condensed ssDNA phase in nanoconfinement.

3. Sharp leading-edge profiles reveal millisecond-scale LLPS kinetics

The sharpness of the leading edge in the ssDNA fluorescence profiles provides direct insight into the kinetics of LLPS nucleation and growth under nanoconfinement. Under the highest flow-rate condition (Fig. 6(a), left), the advancing

wavefront exhibits a steep transition, confined within a ~100 μm-wide region. Upstream of this front, the free ssDNA concentration remains effectively equal to the bulk supply concentration, whereas downstream of the front, free ssDNA is nearly depleted. If free ssDNA were not depleted, adsorption and incorporation into the condensed phase would have already initiated in that region, smoothing the profile.

At the measured flow velocity of ~5 mm s^{-1}, the liquid requires only ~20 ms to traverse this 100 μm transition zone. Thus, incorporation of ssDNA from the dilute phase into the condensed phase must occur within ≲10–20 ms. Any finite delay in LLPS nucleation, growth, or equilibration would broaden the transition zone, which is not observed. The absence of such smearing indicates that nucleation, domain growth, and condensation equilibrate on timescales well below tens of milliseconds.

These reaction times are markedly faster than those typically reported for LLPS formation in bulk (seconds to minutes), suggesting that nanoconfinement accelerates LLPS *via* (i) locally elevated ssDNA concentrations near the wall, (ii) high effective surface densities of H1, and (iii) rapid attainment of local supersaturation that promotes near-instantaneous condensation.

Thus, as illustrated schematically in Fig. 9(a), the nanofluidic geometry uniquely suppresses diffusion limitations, allowing the intrinsic reaction kinetics of LLPS to be directly probed. The ability to resolve such rapid condensation dynamics suggests that nanofluidic LLPS could serve as a new quantitative tool for studying LLPS nucleation under extreme confinement—an experimentally difficult regime for conventional microscopy.

4. Physical origin of the observed film thickness scaling: $\delta \propto Q^{0.3}$

Our experiments revealed that the fluorescence intensity (I) of the ssDNA-rich LLPS film scales with the applied differential pressure (ΔP) as $I \propto \Delta P^{0.34}$ (Fig. 6(c)). While a substantial longitudinal pressure gradient exists within the nanochannel to drive this flow, the local absolute pressure is highly unlikely to affect the phase separation behavior. Both the aqueous fluids and the glass substrate are highly incompressible and rigid, and the applied pressure range (hundreds of kPa) is orders of magnitude too small to thermodynamically shift the LLPS equilibrium. Therefore, the volumetric flow rate (Q)—which is strictly proportional to ΔP and conserved throughout the channel length—is the dominant physical factor governing the system. Consequently, the observed scaling can be directly translated to the flow rate as $I \propto Q^{0.34}$. Because LLPS condensates are characterized by an internally fixed polymer concentration dictated by the binodal boundary of the phase diagram,[29] the fluorescence intensity is a direct proxy for film thickness δ, yielding:

$$\delta \propto Q^{0.34}.$$

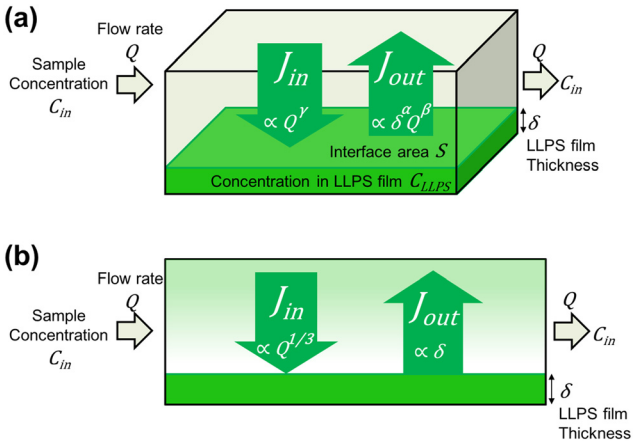

Fig. 9 Steady-state mass balance model for surface-induced LLPS film growth. (a) General framework where the equilibrium film thickness (δ) is determined by the balance between the advective supply flux (J_{in}) and the dissociation efflux (J_{out}). The dependencies of these fluxes on flow rate (Q) and film thickness (δ) are characterized by the exponents γ, α, and β. (b) The specific physical model validated in this study. The influx is governed by diffusion-limited transport following the Lévêque solution (γ = 1/3), while the efflux is dominated by volume-controlled dissociation (α = 1) due to rapid internal diffusion, with negligible shear erosion (β = 0). Balancing these fluxes ($\propto Q^{1/3}$) successfully reproduces the experimentally observed scaling law ($\delta \propto Q^{0.34}$).

To explain the physical origin of this exponent, we constructed a steady-state mass balance model (Fig. 9). Given that δ stabilizes at an equilibrium value, a negative feedback mechanism must govern the film growth. Here, the LLPS film thickness δ is controlled by the balance between (i) advective influx of ssDNA from the dilute bulk ($J_{in} \propto Q^{\gamma}$) and (ii) efflux due to dissociation from the condensate network ($J_{out} \propto \delta^{\alpha} Q^{\beta}$). At steady state:

$$\delta \propto Q^{(\gamma-\beta)/\alpha}.$$

Mathematically, multiple combinations of (α, β, γ) could satisfy the experimental exponent of $(\gamma - \beta)/\alpha \approx 0.34$. However, by incorporating the physicochemical properties of LLPS condensates and our experimental estimates, we demonstrate that the simplest and most physically consistent set of parameters is $\alpha = 1$, $\beta \approx 0$, and $\gamma \approx 0.34$.

4.1 Rapid internal diffusion in LLPS films supports volume-controlled dissociation (α = 1). α is a parameter that determines whether dissociation occurs only at the interface (α = 0) or throughout the entire film, including its interior (α = 1). While dissociation from solid surfaces is typically restricted to the interface (α = 0), biomolecular condensates—particularly electrostatic coacervates like the H1-ssDNA system—are structurally distinct. They are known to possess high water content and form loosely connected polymer networks that are highly permeable to solutes and solvents.[14,29] Wei *et al.* (2017) demonstrated that such condensates behave as low-density hydrogels, allowing rapid internal diffusion of molecules.[28] This implies that dissociation events are not confined to the surface but can occur throughout the film volume (α = 1), provided the

film is sufficiently thin to prevent internal diffusion limitations. We verified this assumption by estimating the film thickness and internal diffusion timescale. Based on typical nucleotide concentrations in polyelectrolyte coacervates (~200 mM),[30] the concentration of dA_{15} strands within the condensed phase is estimated to be approximately 17 mM. In our experiments, the average ssDNA concentration across the entire cross section is below 500 μM, indicating the film thickness δ is extremely thin, likely ≤6 nm. Even assuming a reduced diffusion coefficient within the dense phase ($D_{in} \sim 10^{-11}$ m^2 s^{-1}),[28] the time required for a molecule to diffuse across this thickness is:

$$\tau_{diff} \approx \frac{h^2}{D_{in}} \approx \frac{(6 \times 10^{-9}\ \mathrm{m})^2}{10^{-11}\ \mathrm{m^2\ s^{-1}}} \approx 3.6 \times 10^{-6}\ \mathrm{s}$$

This microsecond-scale diffusion time is orders of magnitude faster than the millisecond-scale phase separation kinetics or the convective transport timescale. Consequently, the chemical potential within the film is uniform, ensuring that the entire film volume is in dynamic equilibrium with the interface. This quantitative assessment strongly validates the bulk dissociation model ($\alpha = 1$).

4.2 Negligibility of shear erosion ($\beta \approx 0$). The contribution of shear-induced erosion (β) was determined to be negligible based on two observations. First, if erosion were significant (*e.g.*, $\beta \approx 1$), satisfying the observed scaling would require an unphysically high supply exponent ($\gamma \approx 1.34$), exceeding even pure convective transport limits. Second, our flow reversal experiments (Fig. 7) revealed that the film does not wash away instantly but retracts slowly with rim formation, a behavior characteristic of high-viscosity fluids.[31] The structural integrity of the condensate, combined with a film thickness (≤6 nm) well within the viscous sublayer, suggests that hydrodynamic lift or shear peeling is minimal ($\beta \approx 0$).

4.3 Physical origin of the observed film thickness scaling: transport-limited growth. With $\alpha = 1$ and $\beta \approx 0$, the scaling relation simplifies to $\gamma \approx 0.34$ (Fig. 9(b)). This result aligns remarkably well with the classical Lévêque solution for diffusion-limited transport in laminar channel flows, which predicts a mass transfer coefficient scaling of $J_{in} \propto Q^{1/3}$.[32] Thus, we conclude that despite the rapid diffusion in nanofluidic confinement, the growth of the H1-ssDNA LLPS film is governed by the physics of the diffusion boundary layer. This demonstrates that the LLPS condensation kinetics are fast enough to immediately consume the flux supplied by rapid radial mixing in nanofluidic channels. It is also consistent with the millisecond-scale LLPS kinetics suggested in discussion section 3. In terms of being "rapid mixing yet diffusion-limited," nanofluidics may be an ideal platform for controlling LLPS film thickness at the 10^0 nm to Å level.

The fact that the system remains diffusion-limited implies that the channel dimension itself acts as a critical parameter governing the rapidity of film formation. This demonstrates that nanofluidics does not merely "miniaturize" the reaction volume but actively enhances the capture efficiency by leveraging the rapid radial diffusion to overcome mass-transport limitations.

5. Peel-off dynamics demonstrate cohesive, finite-thickness LLPS domains

The behavior of the condensed phase upon flow reversal provides some of the strongest evidence for its cohesive, multi-phase nature. When the flow was reversed from right to left, FITC exhibited simple erosion, with the initial profile serving as an envelope that was gradually shaved away. In contrast, ssDNA exhibited a pronounced bulging-and-amplification behavior: the interface advanced upstream as a deformable front, producing a transient amplification of fluorescence before detaching and sweeping downstream (Fig. 1 and 7).

Such behavior is impossible for molecular adsorption layers, which would be removed monotonically. Instead, it is characteristic of a cohesive viscoelastic phase that adheres to the surface while also possessing internal cohesion. The front behaved as a single unit, maintaining its morphology across multiple channels and across a wide range of introduction and removal pressures. This insensitivity to preparation conditions reinforces the conclusion that the observed layer is not a residual plug but a stable condensed LLPS domain.

6. Interpreting the initial plug: removal of excess H1 eliminates catastrophic entrance nucleation

The first introduction of ssDNA produced a channel-blocking plug at every nanochannel entrance, whereas no such plugging occurred after the device was thoroughly rinsed. This dichotomy can be explained by the surface chemistry of H1. Immediately after surface modification, the nanochannel walls likely contained both strongly bound H1 and a substantial population of weakly adsorbed excess H1 molecules. Such multilayer or aggregated H1 patches would raise the local surface density well above the LLPS nucleation threshold, allowing catastrophic local condensation (*i.e.*, a sudden transition to a space-filling phase) at the inlet where ssDNA concentration increases abruptly.

Rinsing removes weakly bound H1, leaving behind only the strongly attached monolayer-level population. This reduces the local LLPS propensity sufficiently to prevent plug formation while still permitting thin-layer condensation along the channel walls. Once rinsing was completed, the system produced highly reproducible introduction and removal behaviors across all experiments, firmly linking the disappearance of plug formation to the reduction of excess H1 surface density.

7. Stability and reusability of the functionalized nanochannels

All the repeated flow cycles demonstrated in this study, including the cyclic operations shown in Fig. 8 and Videos S1–S7, were performed using a single nanofluidic chip that underwent more than 15 cycles of LLPS induction and peel-

off. Notably, among these cycles, the 75 kPa introduction shown in the upper right panel of Fig. 8 was the very first trial, whereas the corresponding 75 kPa introduction in the lower right panel was the final trial performed. The remarkable consistency between these initial and final profiles demonstrates that the covalently immobilized histone H1 layer remained fully intact, showing no significant degradation in its LLPS-inducing performance even after extensive repeated use.

Modeling considerations, limits, and future directions. While the observations are consistently explained by a two-phase LLPS model, several uncertainties remain:

• Surface density and modification efficiency of H1 were not directly quantified in this study. Previous reports utilizing linker-based immobilization within aminosilanized nanochannels achieved surface densities ranging from several hundreds to ~3000 molecules per μm^2 for mouse IgG.[9,10] Assuming the molecular footprint scales with the 2/3 power of the molecular weight ratio between IgG (~150 kDa) and histone H1 (~21 kDa), the 2D surface density of H1 is estimated to be ~10 000 molecules per μm^2. Meanwhile, the accumulated ssDNA is estimated to reach ~6×10^4–9×10^4 molecules per μm^2. While this suggests an accumulation slightly exceeding a strict 1 : 1 stoichiometry, the difference is not on an order of magnitude that allows for a definitive discussion of breaking the 2D capacity limit based solely on these estimations. For this initial proof-of-concept, we intentionally utilized a simple system dominated by strong heterotypic interactions to isolate the fundamental fluidic phenomena. We postulate that in such a system, continuous growth of the LLPS phase far beyond the immobilized H1 amount would likely be restricted. Therefore, a promising future direction is to explore molecular systems that also possess weak homotypic interactions. We hypothesize that such systems hold the potential to form massive LLPS condensates, which could theoretically surpass the quantitative limits of 2D surface-immobilized molecules. Establishing direct quantification methods for the surface seeds will be performed in tandem with these advanced molecular designs. Furthermore, the local H1 density seems not spatially uniform, as evidenced by initial plugging and multimodal steady-state profiles. Controlling this *via* SAM-based patterning will improve reproducibility.

• Thickness δ cannot yet be measured directly, and interpretations rely on fluorescence intensity. TIRF would be highly valuable for direct validation. While establishing a clean evanescent field is optically unfeasible within the tightly confined 3D geometry of the current nanochannels, employing planar, slit-like nanochannels in future device designs would successfully enable the application of TIRF for direct thickness measurements.

• The exponent ~0.3 agrees with mass-transfer-limited theory but current data cannot discriminate between 1/3 scaling and nearby values.

• The reactive timescale (<20 ms) was indirectly estimated from the steepness of the wavefront. This indirect approach stems from the inherent difficulty of directly quantifying the ssDNA concentration in the freely flowing dilute phase. Under submicron confinement, the optical diffraction limit causes the overwhelming fluorescence signal from the massive condensed phase to completely mask the faint signal of the adjacent dilute phase. To overcome this extreme concentration disparity, future studies could employ sparse-labeling techniques (tracking trace amounts of fluorophores within an unlabeled majority) coupled with ultra-high-speed imaging.

• Rheological properties of the condensed phase (viscosity, yield stress, elasticity) are unknown but would help refine peel-off models.

Addressing these limitations will allow nanofluidic LLPS to evolve from phenomenological demonstration toward a predictive, quantitative platform.

Perspectives for applications.

• Downstream handling of the peeled condensates: once the massive LLPS phase is hydrodynamically peeled off, its ultra-high local concentration provides unique analytical opportunities. Future strategies include hydrodynamically transporting and capturing these condensates in specifically patterned downstream regions for highly sensitive *in situ* biochemical analysis, compartmentalizing them into micro-droplets, or utilizing detachable bonding techniques to physically open the device for direct surface characterization.

• Temperature dependence and active thermal control: while all LLPS phenomena in the current study were strictly maintained at an isothermal condition (25 °C) owing to the massive heat capacity of the glass substrate instantaneously absorbing any reaction enthalpy, exploring the temperature dependence of LLPS in nanoconfinement remains a fascinating frontier. Because the reaction rate constants and thermodynamic phase boundaries governing the LLPS condensation are highly sensitive to temperature, integrating on-chip localized thermal control units to establish spatial temperature gradients could theoretically enable the active, programmable spatial profiling of the film thickness (δ) independently of the flow parameters.

• Implementing this LLPS-based continuous system in practical scenarios faces two primary obstacles. First, the structural "scaffold" molecules forming the condensates must be conceptually decoupled from the functional "cargo" molecules. Future designs must employ multi-component systems where an engineered LLPS scaffold selectively partitions specific targets from the flowing phase. Second, simple electrostatic coacervates are highly sensitive to physiological ionic strengths. Ensuring compatibility with complex biological fluids will require utilizing robust, domain-specific interacting molecules or integrating upstream on-chip desalination. Ultimately, by overcoming these challenges, this nanofluidic LLPS platform could evolve into a versatile modular system capable of diverse functions, including selective target enrichment, highly efficient enzymatic reactions, and complex extraction operations *via* dynamic stripping recovery. Functioning as an "organelle-on-a-chip" that mimics natural membraneless organelles, it holds tremendous potential for advanced microanalysis and continuous-flow nanoreactors.

Conclusion

This study provides the first demonstration of flow-programmable, surface-induced LLPS within a nanofluidic channel. Unlike the stochastic and random condensate formation typical of simple bulk mixing, we show that surface-induced LLPS under nanoconfinement is deterministic and can be generated instantaneously with precise spatiotemporal control, establishing it as a controllable platform for dynamic microreactors.

We demonstrated that histone H1-modified nanochannels robustly induce surface-mediated LLPS upon ssDNA introduction. Systematic fluorescence measurements revealed that the formation process is governed by strict physical laws rather than probability: the film thickness followed a specific scaling law ($\delta \propto Q^{0.3}$), suggesting growth governed by diffusion-limited supply within the boundary layer. Furthermore, the condensate exhibited viscous dewetting dynamics—characterized by sharp propagation fronts and peel-off behavior upon flow reversal—confirming its liquid nature and reversible detachability despite high accumulation density. The high surface-to-volume ratio of nanofluidic confinement played a decisive role, enabling the surface to function as a "dominant field" that exhaustively recruits virtually all introduced molecules. This facilitated nucleation and equilibration on millisecond timescales, orders of magnitude faster than typical bulk LLPS kinetics.

These findings indicate that nanofluidic LLPS serves as a promising basis for new classes of dynamic volumetric reactors that combine high capacity, reversible capture, and Ångström-level thickness control. Because functional molecules retain mobility within the 3D phase, this platform could enable high-order functions requiring multi-body interactions, such as substrate channeling. Moreover, the dynamic nature of the condensate opens up operational capabilities that were difficult to achieve with conventional static immobilization: transporting captured molecules *via* hydrodynamic peel-off, replenishing functional molecules on-demand, or refreshing degraded antibodies.

By bridging static surface chemistry with dynamic phase separation, such systems enable engineered analogues of organelle-level processes ("organelle-on-a-chip"), providing a foundation for ultrasensitive biochemical reactions and molecular sieving on a chip.

Author contributions

R. O. performed the experiments, analyzed the results, and wrote the manuscript. Z. Z. fabricated the device and performed the experiments. X. Y. fabricated the device. R. W. performed the experiments. K. M. conceived the project and analyzed the results.

Conflicts of interest

The authors declare no competing interests.

Data availability

The data supporting this article have been uploaded as part of the supplementary information (SI). Additional raw data are available from the corresponding author upon reasonable request. Supplementary information is available. See DOI: https://doi.org/10.1039/d6lc00003g.

Acknowledgements

This work was partially supported by JSPS KAKENHI Grant Number 24K01322.

References

1 G. M. Whitesides, *Nature*, 2006, **442**(7101), 368–373.
2 Y. Song, B. Lin, T. Tian, X. Xu, W. Wang, Q. Ruan, J. Guo, Z. Zhu and C. Yang, *Anal. Chem.*, 2019, **91**(1), 388–404.
3 J. C. Love, L. A. Estroff, J. K. Kriebel, R. G. Nuzzo and G. M. Whitesides, *Chem. Rev.*, 2005, **105**, 1103–1169.
4 F. Rusmini, Z. Zhong and J. Feijen, *Biomacromolecules*, 2007, **8**, 1775–1789.
5 A. D. Stroock, S. K. W. Dertinger, A. Ajdari, I. Mezić, H. A. Stone and G. M. Whitesides, *Science*, 2002, **295**(5555), 647–651.
6 L. Capretto, W. Cheng, M. Hill and X. Zhang, *Top. Curr. Chem.*, 2011, **304**, 27–68.
7 W. Sparreboom, A. Van Den Berg and J. C. T. Eijkel, *Nat. Nanotechnol.*, 2009, **4**, 713–720.
8 R. B. Schoch, J. Han and P. Renaud, *Rev. Mod. Phys.*, 2008, **80**, 839.
9 K. Shirai, K. Mawatari and T. Kitamori, *Small*, 2014, **10**, 1514–1522.
10 R. Ohta, Y. Matsumoto, Y. Itoh and T. Kitamori, in *proc. microtas2021*, 2021, p. 1407.
11 K. Yamamoto, K. Morikawa, H. Imanaka, K. Imamura and T. Kitamori, *Anal. Chem.*, 2022, **94**, 15686–15694.
12 A. W. Peterson, R. J. Heaton and R. M. Georgiadis, *Nucleic Acids Res.*, 2001, **29**, 5163–5168.
13 I. Wheeldon, S. D. Minteer, S. Banta, S. C. Barton, P. Atanassov and M. Sigman, *Nat. Chem.*, 2016, **8**, 299–309.
14 S. F. Banani, H. O. Lee, A. A. Hyman and M. K. Rosen, *Nat. Rev. Mol. Cell Biol.*, 2017, **18**, 285–298.
15 A. A. Hyman, C. A. Weber and F. Jülicher, *Annu. Rev. Cell Dev. Biol.*, 2014, **30**, 39–58.
16 H. X. Zhou, V. Nguemaha, K. Mazarakos and S. Qin, *Trends Biochem. Sci.*, 2018, **43**, 499–516.
17 A. S. Lyon, W. B. Peeples and M. K. Rosen, *Nat. Rev. Mol. Cell Biol.*, 2021, **22**, 215–235.
18 X. Tong, R. Tang, J. Xu, W. Wang, Y. Zhao, X. Yu and S. Shi, *Signal Transduction Targeted Ther.*, 2022, **7**, 221.
19 J. Söding, D. Zwicker, S. Sohrabi-Jahromi, M. Boehning and J. Kirschbaum, *Trends Cell Biol.*, 2020, **30**, 4–14.
20 Y. Lee, S. Park, F. Yuan, C. C. Hayden, L. Wang, E. M. Lafer, S. Q. Choi and J. C. Stachowiak, *Nat. Commun.*, 2023, **14**, 8015.
21 J. A. Ditlev, *J. Mol. Cell Biol.*, 2021, **13**, 319–324.

22 N. A. Erkamp, R. Qi, T. J. Welsh and T. P. J. Knowles, *Lab Chip*, 2023, **23**, 9–24.
23 W. E. Arter, R. Qi, N. A. Erkamp, G. Krainer, K. Didi, T. J. Welsh, J. Acker, J. Nixon-Abell, S. Qamar, J. Guillén-Boixet, T. M. Franzmann, D. Kuster, A. A. Hyman, A. Borodavka, P. S. George-Hyslop, S. Alberti and T. P. J. Knowles, *Nat. Commun.*, 2022, **13**, 7845.
24 S. Dilissen, P. L. Silva, A. Smolentseva, T. Kache, R. Thoelen and J. Hendrix, *Biochim. Biophys. Acta, Gen. Subj.*, 2024, **1868**, 130673.
25 K. W. Y. Chan, M. Navi, J. Kieda, T. Moran, D. Hammers, S. Lee and S. S. H. Tsai, *Lab Chip*, 2022, **22**, 2647–2656.
26 Y. Huang, T. Liu, Q. Huang and Y. Wang, *ACS Sens.*, 2024, **9**, 3466–3488.
27 M. Mimura, S. Tomita, H. Sugai, Y. Shinkai, S. Ishihara and R. Kurita, *Front. Cell Dev. Biol.*, 2021, **9**, 710729.
28 M. T. Wei, S. Elbaum-Garfinkle, A. S. Holehouse, C. C. H. Chen, M. Feric, C. B. Arnold, R. D. Priestley, R. V. Pappu and C. P. Brangwynne, *Nat. Chem.*, 2017, **9**(11), 1118–1125.
29 B. A. Gibson, L. K. Doolittle, M. W. G. Schneider, L. E. Jensen, N. Gamarra, L. Henry, D. W. Gerlich, S. Redding and M. K. Rosen, *Cell*, 2019, **179**, 470–484.e21.
30 E. Spruijt, A. H. Westphal, J. W. Borst, M. A. Cohen Stuart and J. van der Gucht, *Macromolecules*, 2010, **43**, 6476–6484.
31 G. Reiter, *Phys. Rev. Lett.*, 1992, **68**, 75.
32 M. A. Lévêque, *Ann. Mines*, 1928, **13**, 201.